ISSN (Print) 1226-1750
ISSN (Online) 2233-6656
Journal of Magnetics 30(4), 660-671 (2025) https://doi.org/10.4283/JMAG.2025.30.4.660

Electromagnetic Performance Evaluation of a Multi-energy Interface Electric-drive-reconstructed Onboard Charger for EVs

Yuhao Zhang, Feng Yu*, and Linhao Qiu

School of Electrical Engineering and Automation, Nantong University, Nantong 226019, China

(Received 12 June 2024, Received in final form 29 October 2025, Accepted 4 November 2025)

The multi-energy interface electric-drive reconstructed onboard charger (MEI-EDROC) incorporating a six-phase machine represents an emerging technology capable of charging the solar-powered electric vehicle (SPEV) in various modes, encompassing DC charging mode, in-motion charging mode, single-phase charging mode, and three-phase charging mode. Despite the average torque being approximately zero to ensure the machine stationary, the presence of harmonic fluxes in the permanent magnet synchronous machine (PMSM) with fractional slot concentrated winding (FSCW) leads to the pulsating charging torque. Additionally, the MEI-EDROC has a risk of irreversible demagnetization during charging process. In this paper, the electromagnetic performance of the MEI-EDROC is evaluated in detail. Firstly, theoretical calculations and finite element (FE) analysis are conducted to evaluate the electromagnetic torque induced by harmonic fluxes in each charging mode. And then, the iron loss and PMs eddy loss of various operation modes are compared. Moreover, a comprehensive evaluation of PMs irreversible demagnetization in each operation process is carried out. Finally, experimental results of a 2 kW laboratory prototype are provided for further verification.

Keywords : electromagnetic performance evaluation, Multi-energy interface electric-drive-reconstructed onboard charger (MEI-EDROC), six-phase machine

1. Introduction

In most electric vehicles (EVs), the drive system operates independently of the charging system, resulting in an increase in both volume and weight [1-3]. To tackle these issues, the implementation of an electric-drive-reconstructed onboard charger (EDROC) is proposed in [4, 5]. The functions of the power converter can be greatly integrated by reutilizing the driving system components for charging, thereby enhancing the utilization rate of on-board equipment and resulting in effective cost reduction. Subsequent to that, comprehensive investigations have been carried out on EDROC, leading to the proposition of diverse topologies [6-8].

In terms of the EDROC incorporating a multiphase machine, zero-average torque generation during charging can be ensured [9], thereby improving the system security. As a type of multiphase machine, the six-phase machine is a highly appealing option for EDROC applications, which is mainly attributed to reconfiguring two sets of *dq*-axis currents for torque cancellation [10]. The choice of a six-phase machine for the EDROC is deliberate and is driven by several critical requirements that are not adequately met by conventional three-phase machines or other multiphase configurations. Firstly, it provides a greater number of controllable degrees of freedom compared to a three-phase system. This is essential for independently managing propulsion torque and charging currents, especially for realizing complex multi-mode operations like in-motion charging. Secondly, the specific asymmetrical six-phase structure (with two sets of three-phase windings displaced by 30 electrical degrees) enables the generation of three distinct subspaces (α-β, x-y and 0_1-0_2). This inherent decoupling is strategically leveraged to inject zero-sequence currents for charging in several modes without interfering with the fundamental torque-producing α-β subspace. While higher-phase-count machines (e.g., nine-phase) offer even more control freedom, the six-phase configuration represents an optimal trade-off, providing sufficient control redundancy

*The work was supported by the National Natural Science Foundation of China (52177051).
Corresponding author: Tel: +86-13776929955
e-mail: yufeng628@ntu.edu. cn

for the targeted charging modes without unduly increasing the power converter complexity and system cost. [11] proposed an EDROC topology incorporating a six-phase machine. This topology, however, can only achieve zero torque at some specific rotor positions during the three-phase charging mode. In order to ensure zero charging torque at any rotor positions, [12] proposed a new winding configuration that can avoid torque generated by fundamental flux. Nevertheless, the harmonic flux components of PMs remain and result in torque ripple [13, 14] proposed a multi-energy interface electric-drive reconstructed onboard charger (MEI-EDROC) for solar-powered electric vehicle (SPEV). This topology enables functionalities such as DC charging, propulsion, in-motion charging, and single-phase charging while ensuring zero-average torque. However, this literature does not consider the pulsating torque caused by the injection of the zero-sequence current (ZSC) which is utilized to realize charging operation. In essence, the pulsating torque generation is due to the existence of 3rd harmonic flux [15].

Apart from the number of machine phases, the choice of slot and pole combination is also vital when it comes to the EDROC. The combination of 12 slots and 10 poles in the fractional slot concentrated winding (FSCW) configuration demonstrates enhanced winding factor and reduced rotor losses during both propulsion and charging operations [13]. Nevertheless, it is still possible to detect sub and super-synchronous harmonic flux components which cannot be fully eliminated as in a distributed winding configuration. These elements contribute to excessive heat generation, resulting in reduced efficiency and irreversible demagnetization of PMs [16]. Therefore, it is necessary to evaluate the loss and demagnetization of the EDROC incorporating a FSCW machine during charging process.

In the past few years, significant efforts have been dedicated to emphasizing the demagnetization analysis of PMSMs and induction machines [17, 18]. The demagnetization characteristics of SPM and IPM machines were comprehensively studied in [17]. Likewise, another analysis on demagnetization effects in an IPM-type machine is conducted in [18]. Nevertheless, these studies solely focus on the propulsion mode. Except for this, [13] analyzed the demagnetization effect in three-phase charging mode. However, most of the existing studies are limited to specific charging modes or fail to comprehensively address the electromagnetic performance under multiple charging scenarios. For instance, while [11] ensures zero torque only at specific rotor positions, and [12] mitigates fundamental torque but neglects harmonic-induced pulsations, the multi-mode operation capability and its associated challenge, such as harmonic flux-induced torque ripple, loss distribution, and irreversible demagnetization across all charging mode, have not been systematically evaluated. Moreover, previous works often overlook the combined effects of zero-sequence current injection and high-temperature operation on PM demagnetization in a six-phase FSCW-PMSM based MEI-EDROC. To bridge these research gaps, this paper presents a comprehensive electromagnetic performance evaluation of the MEI-EDROC, considering all its operational modes. The proposed approach not only theoretically and experimentally analyzes the torque components induced by harmonic fluxes but also evaluates the core loss, PM eddy loss, and demagnetization risk under each charging mode, which have been largely neglected in prior arts.

The main contributions of this work, in comparison with existing studies on EDROC, are outlined as follows:

(1) A theoretical calculation method for electromagnetic torque under different charging modes is proposed, which for the first time incorporates the influence of harmonic flux components.

(2) A systematic demagnetization analysis and loss evaluation are performed for various operational modes, supported by corresponding finite-element (FE) simulations that validate the theoretical models.

(3) Comprehensive experimental validation is conducted on a 2 kW prototype machine, covering DC, in-motion, and three-phase charging scenarios. Moreover, an innovative approach using the input voltage spectrum is introduced to assess the extent of demagnetization after prolonged charging operation.

The remainder of the paper is structured as follows. The various charging modes of the MEI-EDROC are illustrated in Section II, and the corresponding electromagnetic torques are theoretically calculated in Section III, accompanied by related FE results. Section IV evaluates the losses and the demagnetization of each operation mode. Finally, the experimental results that confirm the above analysis are presented in Section V, and Section VI gives the overall conclusion of this paper.

2. Topology and Operation Modes Analysis

The configuration of the MEI-EDROC is illustrated in Fig. 1. The key components of the system comprise a six-phase PMSM with two neutral points, a battery, a six-phase two-level inverter, an additional set of five mode switches (S1-S5), a collection of VRPP, and a digital control system. The energy sources interfacing with the

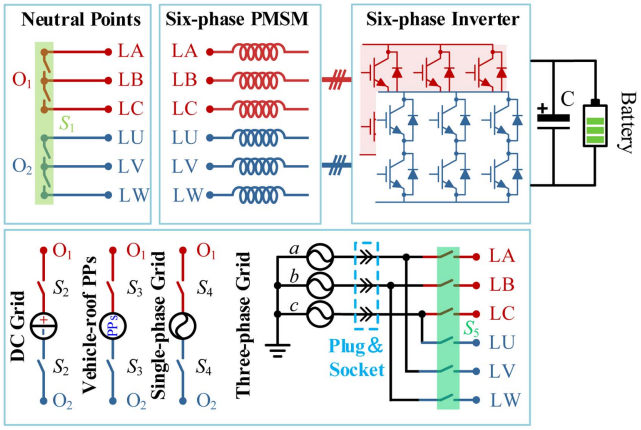

Fig. 1. (Color online) Interior permanent-magnet synchronous machine.

charger are specified as follows to clarify the operational context: the battery pack is rated at a nominal voltage of 144V, representing a typical low-voltage EV battery system; the VRPP (e.g., an integrated solar panel array) is characterized by an output voltage range of 36-72V and a maximum power point around 600W, simulating realistic renewable energy input; the DC grid is represented by a 100V DC power supply; and the single-phase/three-phase AC grids operate at standard voltages of 220V AC. These specifications align with the power level of the 2 kW prototype machine and are representative of common low-power charging scenarios. It encompasses five operation modes: (1) propulsion mode, (2) DC charging mode, (3) in-motion charging mode, (4) single-phase charging mode, and (5) three-phase charging mode. Extensive research has been conducted on the propulsion mode, and hence it will not be further discussed in this context.

2.1. DC Charging Mode

When the EV operates in the DC charging mode, switch S_1 is closed. By closing either switch S_2 or switch S_3, the DC grid or the VRPP can be connected to the two neutral points. To regulate the voltage of the VRPP or the DC grid to achieve the desired charging level, a six-phase inverter and a six-phase PMSM are reutilized as a Boost converter. It should be noted that this circuit can be analogous to two boost converters connected in series and designed for regulating charging current/voltage [14].

2.2. In-motion Charging Mode

To achieve the in-motion charging mode, switches S_1 and S_3 are activated, facilitating the connection of the VRPP to two neutral points. As long as the output power of the VRPP reaches a sufficiently high level, the system will operate in the mode of in-motion charging. The output energy of the VRPP is not only utilized for propulsion, but also for simultaneous battery charging. The six-phase inverter functions as both the machine driver and the regulator for maximum power point tracking (MPPT) operation in the VRPP.

2.3. Single-phase Charging Mode

In this operation mode, the connection between the two neutral points of the machine is established by closing switches S_1 and S_4, thereby integrating the single-phase grid. The six-phase drive is reconfigured into a triple-parallel single-phase H-bridge rectifier. The single-phase grid voltage is rectified and regulated by the H-bridge rectifier to facilitate battery charging.

2.4. Three-Phase Charging Mode

In the three-phase charging mode, the six-phase machine windings are reutilized as filter inductors, with only S_5 being closed. Evidently, the grid phases *a*, *b*, and *c* are interconnected with the machine phases *A*, *B*, and *C* correspondingly. It is noteworthy that the grid phases *a*, *b*, and *c* are concurrently linked to the machine phases *V*, *W*, and *U*. This distinctive winding configuration has been devised to eliminate the electromagnetic torque during the charging process [12].

3. Electromagnetic Torque Evaluation

When the MEI-EDROC operates in charging modes, irrespective of the specific charging mode employed, the currents flowing through the machine windings differ from those observed in propulsion mode. The generation of electromagnetic torque poses a significant threat to the reliability of the system. Moreover, even a stationary machine has the potential to generate an unfavorable torque that compromises system safety. Therefore, it is imperative to explore methods for its theoretical elimination.

According to the theory of magnetic co-energy [11], the electromagnetic torque T_e can be derived as

$$T_e = \frac{\partial W_{co}}{\partial \theta_e} = n_p\left(\frac{\partial}{\partial \theta_e} i_s^T \psi_s + \frac{1}{2} i_s^T \frac{\partial L_s}{\partial \theta_e} i_s\right) \tag{1}$$

where W_{co} is the co-energy, i_s is the machine current matrix, n_p is the number of pole pairs, θ_e is the electrical angle, and ψ_s is the PM flux. According to (1), the torque is primarily influenced by the flux and phase currents. Therefore, the corresponding analysis of them under different charging modes constitutes a crucial step in evaluating the torque. It is noteworthy that the machine

employed in this study is a surface mounted PMSM, thereby excluding the consideration of the reluctance torque.

3.1. Charging Torque in DC Charging Mode

Considering the 3rd harmonic flux, the PM flux can be expressed as

$$\psi_s = \begin{bmatrix} \psi_{f1}\cos\theta_e + \psi_{f3}\cos 3\theta_e \\ \psi_{f1}\cos(\theta_e - 2\pi/3) + \psi_{f3}\cos 3\theta_e \\ \psi_{f1}\cos(\theta_e + 2\pi/3) + \psi_{f3}\cos 3\theta_e \\ \psi_{f1}\cos(\theta_e - \pi/6) + \psi_{f3}\cos(3\theta_e - \pi/2) \\ \psi_{f1}\cos(\theta_e - 5\pi/6) + \psi_{f3}\cos(3\theta_e - \pi/2) \\ \psi_{f1}\cos(\theta_e + \pi/2) + \psi_{f3}\cos(3\theta_e - \pi/2) \end{bmatrix} \quad (2)$$

where ψ_{f1} is the amplitude of fundamental flux, and ψ_{f3} is the amplitude of 3rd harmonic flux.

The machine windings exclusively carry DC currents in this mode, thereby enabling the expression of winding currents i_s as

$$i_s^T = \frac{1}{3}\left[-I_{DC} \quad -I_{DC} \quad -I_{DC} \quad I_{DC} \quad I_{DC} \quad I_{DC}\right] \quad (3)$$

where I_{DC} is the value of the DC current. By substituting (2) and (3) into (1), the electromagnetic torque produced in this mode can be derived as

$$T_e = \frac{3\sqrt{2}}{2} n_p I_{DC} \psi_{f3} \sin(3\theta_e + \frac{\pi}{4}) \quad (4)$$

In this mode, the machine remains stationary, and a constant torque is generated merely in relation to the position of the rotor. The FE results of the electromagnetic torque generated at I_{DC} = 15A are illustrated in Fig. 2(a), where θ_m represents the mechanical angle. Obviously, the FEA results are consistent with those derived in (4). And it can be observed that the torque will be eliminated when θ_e = -π/12+kπ/3 ($k \in$ Z).

3.2. Charging Torque in In-motion Charging Mode

When the EV operates in the in-motion charging mode, both propulsion currents and the ZSC are flowing through the machine windings. Correspondingly, the winding currents can be expressed as

$$i_s = \begin{bmatrix} -I_{DC}/3 + i_A \\ -I_{DC}/3 + i_B \\ -I_{DC}/3 + i_C \\ I_{DC}/3 + i_U \\ I_{DC}/3 + i_V \\ I_{DC}/3 + i_W \end{bmatrix} \quad (5)$$

where i_X (X=A, B, …, W) is the propulsion current.

For the purpose of simplifying calculations, vector space decomposition (VSD) is employed to streamline the mathematical model of a six-phase asymmetrical PMSM. The transformation matrix T_{VSD}, which facilitates decoupling, can be mathematically represented as

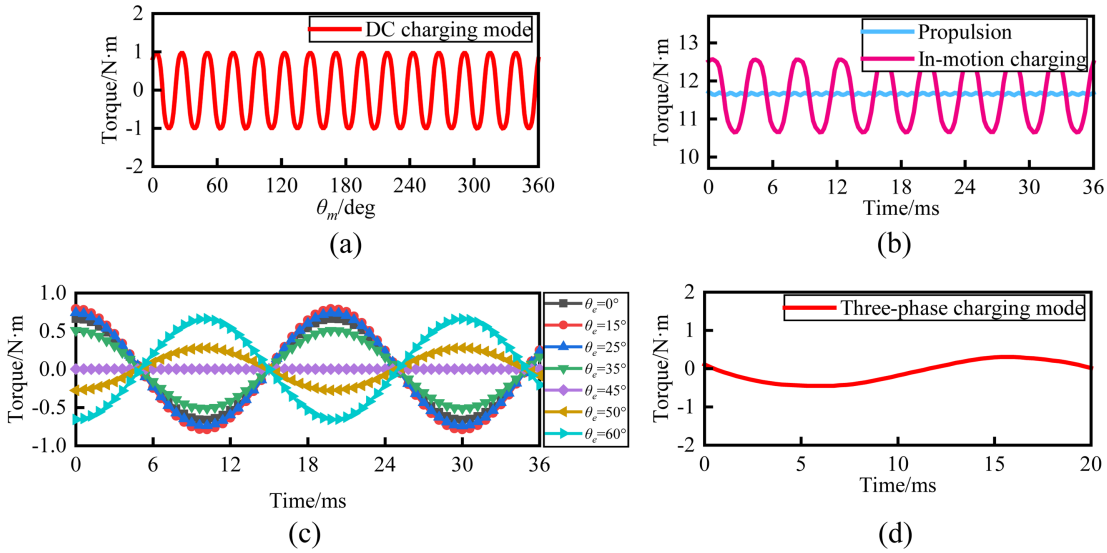

Fig. 2. (Color online) FE results of torque. (a) DC charging mode under various angles. (b) In-motion charging mode and propulsion mode. (c) Single-phase charging mode under various angles. (d) Three-phase charging mode.

$$T_{\mathrm{VSD}}=\frac{1}{3}\begin{bmatrix}1 & -1/2 & -1/2 & \sqrt{3}/2 & -\sqrt{3}/2 & 0\\ 0 & \sqrt{3}/2 & -\sqrt{3}/2 & 1/2 & 1/2 & -1\\ 1 & -1/2 & -1/2 & -\sqrt{3}/2 & \sqrt{3}/2 & 0\\ 0 & -\sqrt{3}/2 & \sqrt{3}/2 & 1/2 & 1/2 & -1\\ 1 & 1 & 1 & 0 & 0 & 0\\ 0 & 0 & 0 & 1 & 1 & 1\end{bmatrix}\begin{matrix}\alpha\\ \beta\\ x\\ y\\ 0_1\\ 0_2\end{matrix} \quad (6)$$

The mathematical model is transformed from the natural coordinate system to the α-β, x-y, and 0_1-0_2 subspaces through the VSD transformation.

Similarly, the T_e produced in this mode can be derived as

$$T_e=3n_p i_q[i_d(L_d-L_q)+\psi_{f1}]-\frac{9\sqrt{2}}{2}n_p i_{01}\psi_{f3}\sin(3\theta_e+\frac{\pi}{4}) \quad (7)$$

where the L_d and L_q are the d-axis and q-axis inductance of the PMSM respectively.

The FE results presented in Fig. 2(b) illustrate the electromagnetic torque generated during the in-motion charging mode and propulsion mode, with I_{DC} at 15A, the amplitude of i_X at 12A, and machine speed at 1000RPM. It is observed that the average torque of the in-motion charging mode, approximately 11.6N·m, closely matches that of the propulsion mode. However, a significant torque ripple of about 6.33 % is introduced by the ZSC in comparison to the smooth operation of propulsion mode, which poses as an adverse factor for the system.

C. Charging Torque in Single-phase Charging Mode

In the single-phase charging mode, zero-sequence alternating currents flow through the windings, resulting in the generation of pulsating torque. The expression of the winding currents in this mode can be formulated as

$$i_s=\begin{bmatrix}-(I_{sg}\cos\omega_{sg}t)/3\\ -(I_{sg}\cos\omega_{sg}t)/3\\ -(I_{sg}\cos\omega_{sg}t)/3\\ (I_{sg}\cos\omega_{sg}t)/3\\ (I_{sg}\cos\omega_{sg}t)/3\\ (I_{sg}\cos\omega_{sg}t)/3\end{bmatrix} \quad (8)$$

where I_{sg} is the amplitude of the single-phase currents, and ω_{sg} is the angular frequency of single-phase grid. Similarly, by substituting (8) and (2) into (1), the T_e generated in this mode can be derived as

$$T_e=\frac{\sqrt{2}}{2}n_p I_{sg}\psi_{f3}\cos\omega_{sg}t\sin(3\theta_e+\frac{\pi}{4}) \quad (9)$$

The FE results of the torque are presented in Fig. 2(c) with I_{sg} = 12A. It is evident that the results align with (9). The fluctuation of torque varies at different rotor positions. Moreover, similar to the DC charging mode, the existence of specific rotor positions (θ_e = -π/12+kπ/3) where the torque can be nullified is also observed.

3.3. Charging Torque in Three Phase Charging Mode

This charging mode utilizes the x-y subspace to achieve balanced three-phase grid currents with zero-average electromagnetic torque [12]. The resultant subspace currents can be derived as

$$I_m=I_g\sec(\pi/12)/2 \quad (10)$$

$$i_{\alpha\beta xy0_1 0_2}=\begin{bmatrix}0\\ 0\\ I_m\cos(\omega_g t-\pi/12)\\ I_m\cos(\omega_g t+5\pi/12)\\ 0\\ 0\end{bmatrix} \quad (11)$$

where I_g is the amplitude of three-phase grid currents, I_m is the amplitude of phase currents, and ω_g is the angular frequency of three-phase grid. It is obvious that i_α, i_β, i_{01} and i_{02} are equal to zero. Traditionally, it is believed that zero electromagnetic torque can be achieved as long as the i_α and i_β are zero. However, in practical machines, PM flux includes not only fundamental components but also harmonic components, thereby resulting in pulsating torque. In this paper, 5th harmonic flux existing in x-y subspace is taken into consideration. Accordingly, the resultant torque can be derived as

$$T_e=-7.5n_p I_m\psi_{f5}\sin(\omega_g t+5\theta_e-\pi/12) \quad (12)$$

where ψ_{f5} is the amplitude of 5th harmonic flux.

The corresponding result, which is drawn when I_m = 12A and θ_e=0°, is depicted in Fig. 2(d). The torque waveform is almost a sine wave, which is consistent with the calculated result in (12).

4. Evaluation of Loss and Demagnetization

Fig. 3 shows the magnetic field distribution of the PMSM in different operation mode. Comparing Fig. 3(a) with Fig. 3(b), the magnetic vector potential of the in-motion charging mode is higher than that of the propulsion mode. This is due to the fact that the DC magnetization induced by the additional ZSC either amplifies or demagnetizes the magnetic field of the machine. As depicted in Fig. 3(c), it can be concluded that a magnetic field loop is formed by the stator

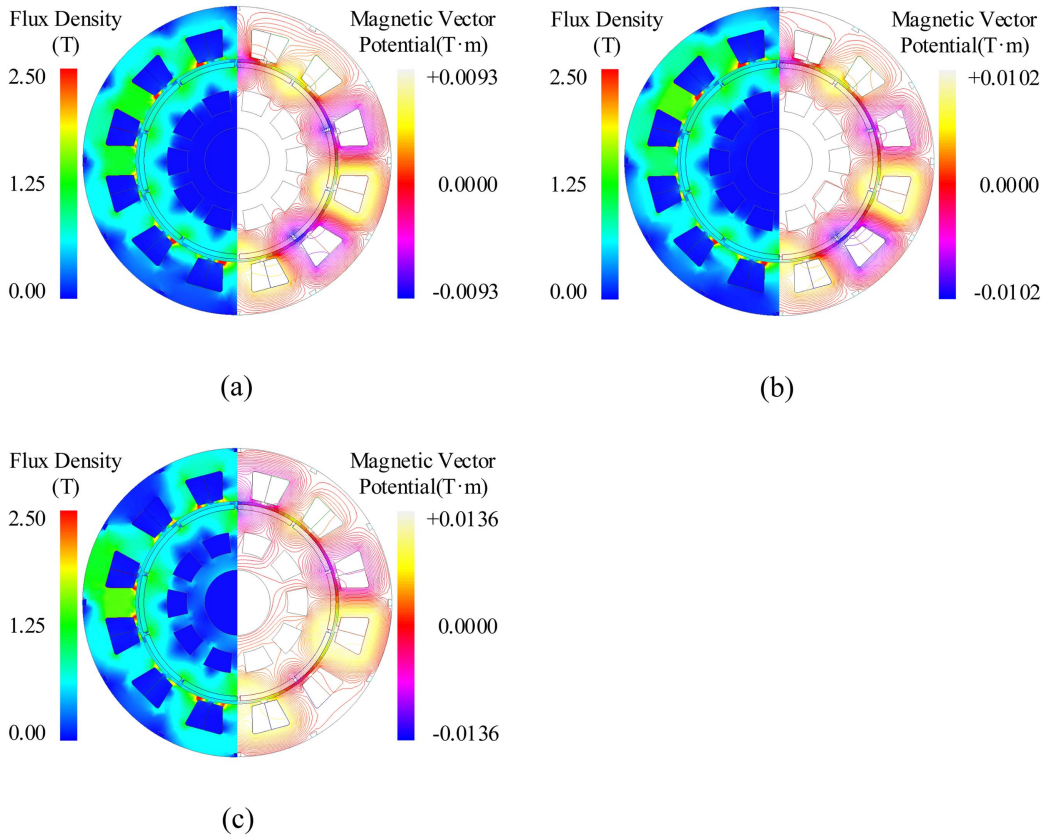

Fig. 3. (Color online) Magnetic field distributions of the machine under different operation modes. (a) Propulsion mode. (b) In-motion charging mode. (c) Three-phase charging mode.

magnetic field and the permanent magnetic field, which are generated by the charging currents and the PMs, respectively. Thus, it is necessary to evaluate the loss and demagnetization of various charging modes.

4.1. Evaluation of Core Loss and PM Eddy Loss

Conventionally, the machine core loss P_{fe} is estimated by the Bertotti's model with three terms: hysteresis loss P_h, eddy current loss P_c, and anomalous loss P_a, as

$$P_{fe} = P_h + P_c + P_a = k_h f B_m^{\alpha} + k_c f^2 B_m^2 + k_a f^{1.5} B_m^{1.5} \tag{13}$$

where f is frequency, B_m is flux density amplitude, k_h, k_c, k_a, and α are the steel hysteresis, eddy current, anomalous loss coefficients, and Steinmetz coefficient, respectively.

When the system operates in the in-motion charging mode, the DC-Biased magnetic induction, which is generated by the output DC current of VRPPs, should be taken into consideration. Accordingly, (13) should be modified as

$$P_{fe} = C_{\mathrm{DC}} k_h f {B_m}^{\alpha} + k_c f^2 {B_m}^2 + k_a f^{1.5} {B_m}^{1.5} \tag{14}$$

$$C_{\mathrm{DC}} = \sqrt{\frac{K_{\mathrm{DC}} |B_{\mathrm{DC}}|}{B_m} + 1} \tag{15}$$

where B_{DC} is the DC flux component, C_{DC} is the DC correction coefficient, and K_{DC} is the DC coefficient.

PM eddy loss P_{eddy} can be estimated by time-stepping FE method as

$$P_{eddy} = \sum_n \left(\int \frac{|J_n|^2}{2\sigma} dv \right) \tag{16}$$

where J_n is the nth harmonic eddy current amplitude, σ and v are conductivity and volume, respectively.

It should be emphasized that the copper loss incurred during each charging mode is solely dependent on the machine's dimensions and input power. Thus, this paper will not delve into an analysis of the copper loss.

The core loss and PM eddy loss of various operation modes are illustrated in Fig. 4. With reference to Fig. 4(a), neither iron loss nor PM eddy loss will be produced in the DC charging mode. This phenomenon can be attributed to the constant DC currents and no alternating

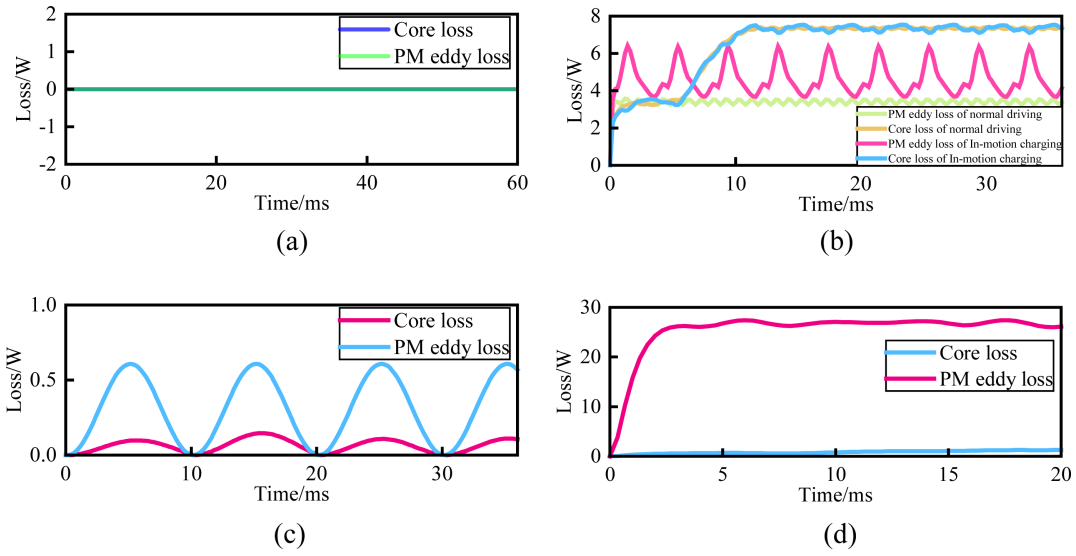

Fig. 4. (Color online) Core loss and PM eddy loss of various operation mode. (a) DC charging mode. (b) In-motion charging mode and propulsion mode. (c) Single-phase charging mode. (d) Three-phase charging mode.

magnetic field. The average core loss of the propulsion mode and the in-motion charging mode are nearly identical, as depicted in Fig. 4(b). Nevertheless, this situation varies when it comes to the PM eddy loss. Actually, an increase occurs in the average PM eddy loss of the in-motion charging mode. The primary factor is that, during the in-motion charging mode, the constant variation of rotor position results in a continuous alteration of the magnetic field loop formed by the PM field and the DC magnetic field. The losses in single-phase charging mode are depicted in Fig. 4(c), wherein both iron loss and eddy current loss exhibit negligible magnitudes. It is noteworthy that the PM eddy loss surpasses the core loss significantly in three-phase charging mode, as illustrated in Fig. 4(d). This observation implies the occurrence of a relatively substantial eddy current within the PMs, which adversely affects the system's efficiency.

4.2. Evaluation of Irreversible Demagnetization

EVs traction machines usually employ conductors with electrical insulation class B or higher (class F or H) which poses an impact on operating temperature [19]. During prolonged operations, it is plausible for the operating temperature to exceed 130 °C. Particularly, during the in-motion charging mode, the amplitudes of phase currents exhibit an increase [22]. And this elevation poses a higher risk of demagnetization on PMs. This study investigates the demagnetization risk of PMs in each charging mode beyond 130 °C, a parameter commonly employed in EV-related research [20, 21].

The variable, named as the demagnetization coefficient, is defined in order to more accurately assess the level of demagnetization. The calculation of this coefficient can be derived using (17).

$$D_c = B_{r1}/B_{r0} \tag{17}$$

where B_{r0} and B_{r1} are residual magnetization before and after demagnetization as shown in Fig. 5, respectively. For a detailed explanation, the demagnetization will be significantly severe when the D_c approaches zero.

The demagnetization results of the propulsion mode and in-motion charging mode at 140 °C and 150 °C are presented in Fig. 6. Notably, for both operation modes, the amplitude of the propulsion current is 12A and the machine speed is 1000RPM. The VRPP output current reaches 15A during in-motion charging mode. The worst

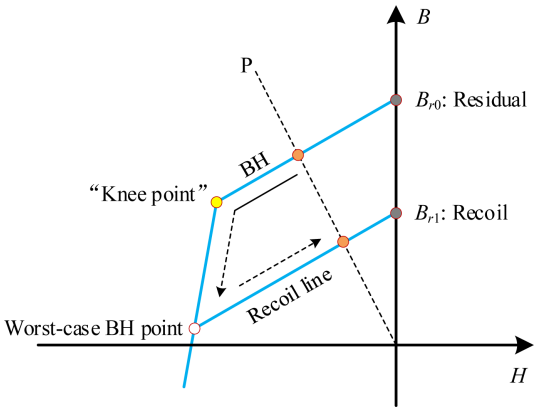

Fig. 5. (Color online) Schematic diagram of demagnetization.

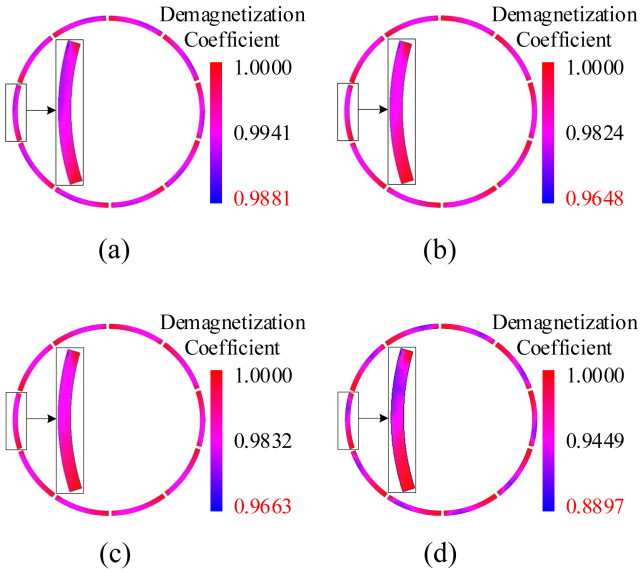

Fig. 6. (Color online) Demagnetization results under different operation modes and temperatures. (a) Propulsion mode at 140 °C. (b) Propulsion mode at 150 °C. (c) In-motion charging mode at 140 °C. (d) In-motion charging mode at 150 °C.

demagnetization coefficients of the in-motion charging mode and the propulsion mode at 150 °C are found to be 0.8897 and 0.9648, respectively. Notably, the in-motion charging mode exhibits a D_c value below the 0.9 safety threshold, indicating a high risk of irreversible demagnetization, while the propulsion mode remains within the acceptable range. It can be concluded that the degree of demagnetization is aggravated by the injection of the ZSC. Thus, in the case of high temperature, it is imperative to restrict the output current of VRPP to mitigate irreversible demagnetization.

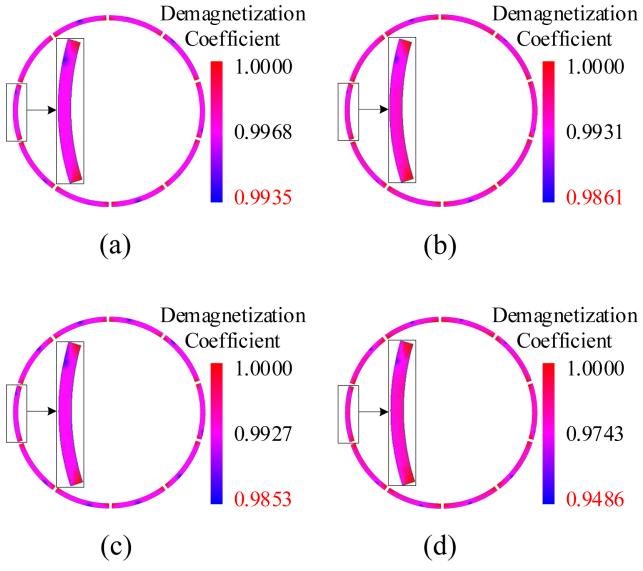

Fig. 7. (Color online) Demagnetization results under different operation modes and temperatures. (a) Single-phase charging mode at 140 °C. (b) Single-phase charging mode at 150 °C. (c) Three-phase charging mode at 140 °C. (d) Three-phase charging mode at 150 °C.

The demagnetization results of single-phase and three-phase charging modes at 140 °C and 150 °C are presented in Fig. 7. Both charging modes exhibit a grid current amplitude of 12A. It can be inferred from the figure that the demagnetization severity is more pronounced in the case of the three-phase charging compared to another at identical temperatures. Actually, the risk of demagnetization is elevated in the three-phase charging mode due to its higher charging power. Under the condition of meeting the basic charging power, both single-phase charging and three-phase charging can achieve $D_c > 0.9$, which is within the acceptable range.

5. Experimental Verifications

5.1. Experimental Setup

In order to assess the practicality and efficiency of the proposed MEI-EDROC, a test setup is conducted, as depicted in Fig. 8. A 2kW six-phase PMSM is utilized as the traction machine for an EV, and its key parameters can be found in Table 1. The load on the machine is generated by employing a magnetic powder brake. To simulate various scenarios such as VRPPs, emerging DC grid, and single-phase grid, two series-connected PPs rated at 36V/300W each are used along with a 100V DC power supply and an AC power source. The MEI-EDROC incorporating six Infineon FF300R12ME4 IGBT modules has been developed. Specifically, in the three-phase charging experiment, an adjustable resistance box setting to 25W is used to consume electric energy, which simulates the charging process of the battery.

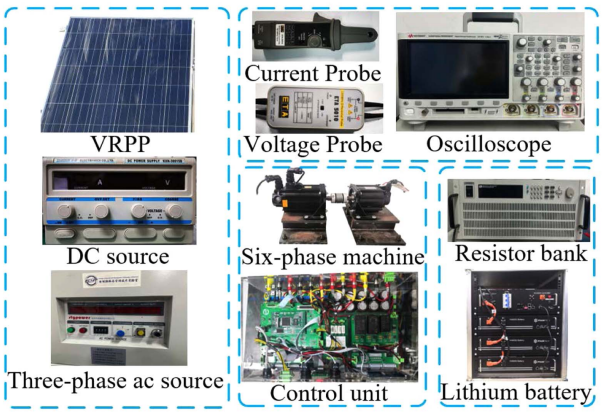

Fig. 8. (Color online) Experimental prototype.

Table 1. Main parameters of the six-phase PMSM.

Parameters	Values
Rated power	2.0kW
Rated speed	2000RPM
Number of pole pairs	5
Direct axis inductance	1.18mH
Quadrature axis inductance	1.13mH
Phase resistance	0.3Ω
Stator-PM magnetic flux	0.082Wb

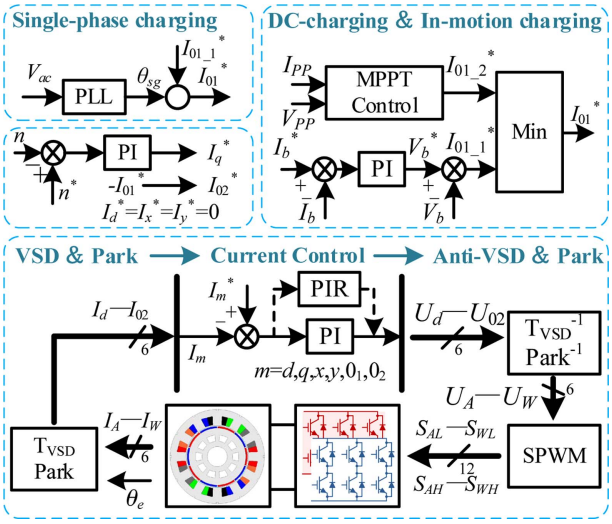

Fig. 9. (Color online) Controller diagram for DC-charging, in-motion charging, and single-phase charging modes.

To ensure the secure and stable operation of each charging mode, the control strategies are depicted in Fig. 9 and Fig. 10, respectively. Among them, Fig. 9 illustrates the integrated control strategy for the three charging modes [14]. The key lies in regulating 0_1-axis current for battery charging while employing traditional field-oriented

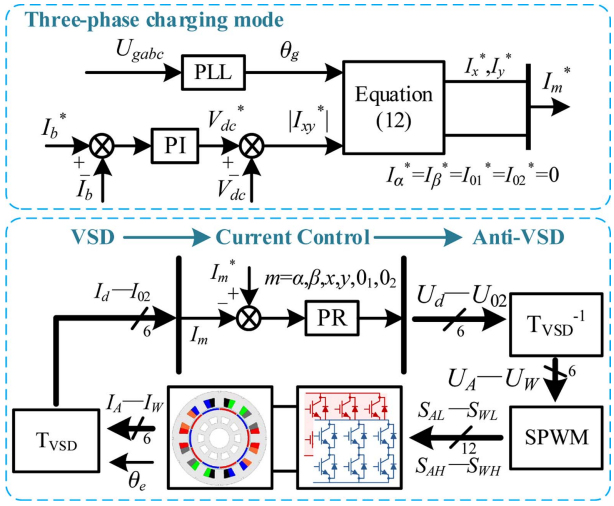

Fig. 10. (Color online) Controller diagram for three-phase charging mode.

control to regulate the machine speed. Particularly, a proportional-integral-resonance (PIR) controller is utilized to regulate the 0_1-axis current in single-phase charging mode, ensuring it closely tracks the sinusoidal reference value. Moreover, the implementation of MPPT utilizes an adaptive perturb and observe MPPT control when the VRPPs are connected. Fig. 10 demonstrates the control strategy for the three-phase charging mode, primarily involving a phase-locked loop (PLL) to achieve unity power factor operation on the grid side and proportional-resonant (PR) controllers to govern subspace currents [12].

5.2. Experiment results

Fig. 11 depicts the steady-state experimental results of the DC charging mode, where the DC power supply is utilized. The charging voltage of the battery is 150 V, and the charging current can follow the set value 2A, which

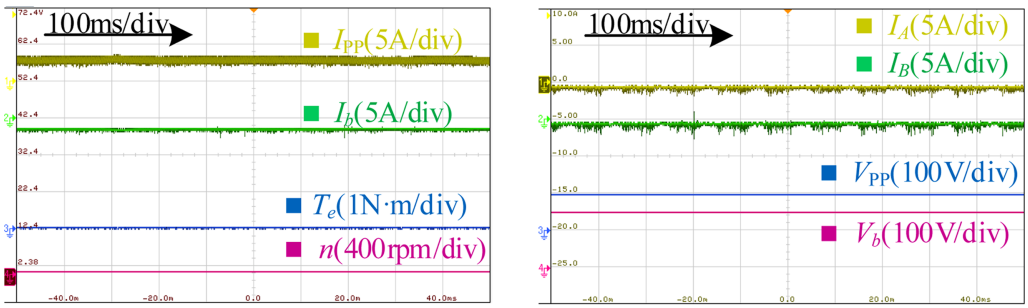

(a) (b)

Fig. 11. (Color online) Experimental results of DC charging mode. (a) VRPP output current I_{PP}, charging current I_b, torque and machine speed. (b) Phase currents I_A, I_B, VRPP voltage V_{PP} and charging voltage V_b.

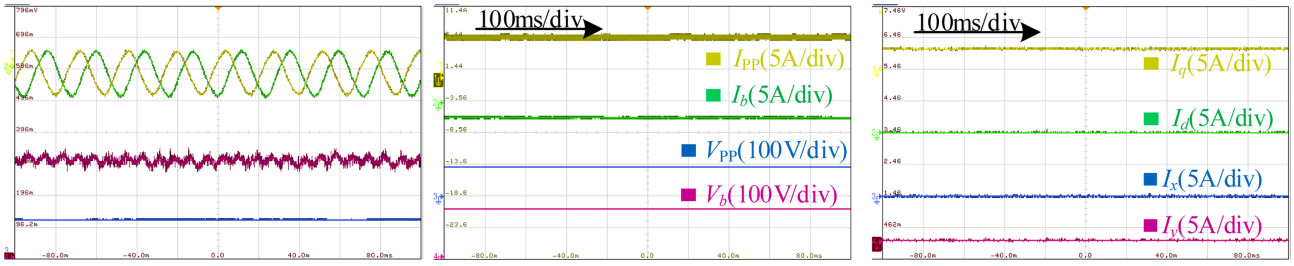

(a) (b) (c)

Fig. 12. (Color online) Experimental results of in-motion charging mode. (a) Phase currents I_A, I_B, torque and machine speed. (b) Charging current/voltage, VRPP output current/voltage (c) Subspace currents I_d, I_q, I_x, and I_y.

meets the basic requirements of battery charging. In the process of DC charging, each winding carries an equal current and produces negligible torque, resulting in no rotation of the machine and ensuring system safety.

The VRPPs are exposed to a condition of 1050 W/m^2 and 25 ºC in the in-motion charging mode. The experimental results of steady-state operation in the in-motion charging mode are depicted in Fig. 12. As shown in Fig. 12(a), the machine operates at a speed of 500RPM with a load of 3N·m. As a result of injection of the 0_1-axis current, the phase currents exhibit a certain DC bias, leading to 3rd pulsation in the output torque, which is approximately 0.3N·m. Fig. 12(b) illustrates that the battery's charging current can effectively track the set value of 2.8A and the charging voltage is 155V. The charging requirements of the battery can be fulfilled. Additionally, as depicted in Fig. 12(c), i_d, i_x, and i_y are all equal to zero, avoiding additional losses. The subspace current i_q can smoothly track the reference value, thereby satisfying the requirements for propulsion.

The experimental results of the three-phase charging mode are presented in Fig. 13. As illustrated in Fig. 13(a), the phase of the grid current can closely track that of the grid voltage due to the effect of PLL. The magnitudes of phase currents A and V are identical and the phase difference is 30º. The subspace currents i_x and i_y display a phase difference of 90º and closely track the desired values, as depicted in Fig. 13(b). Notably, the torque generated during the three-phase charging mode is virtually zero, ensuring machine stability throughout the experiment for safe charging. Additionally, as shown in the Fig. 13(c), i_α, i_β, i_{01} and i_{02} are approximately zero.

5.3. Demagnetization results

The direct measurement of the PMs demagnetization in a PMSM is challenging. The most effective approach to identify demagnetization is through the examination of the machine's stator input voltages or currents. The occurrence of demagnetization in the PMs after extended testing in the charging mode is assessed by conducting an analysis on the frequency spectrum of the filtered input voltage. Research has demonstrated that PMSMs with FSCW experiencing partial demagnetization exhibit additional even-order harmonics (2nd and 4th) in the input voltage signals. Moreover, as demagnetization severity increases, there is a decrease in the magnitude of fundamental harmonic [13].

The input voltage spectrum of the machine with 50% demagnetization of the two magnets (FEA results) and the input voltage spectrum after a long in-motion charging

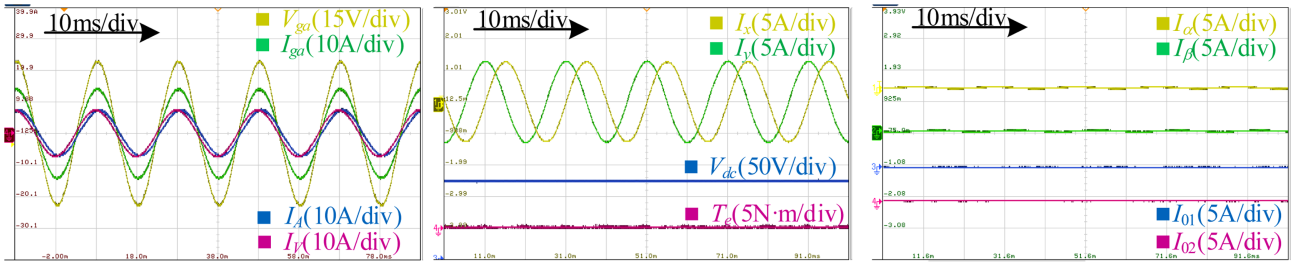

(a) (b) (c)

Fig. 13. (Color online) Experimental results of three-phase charging mode. (a) Grid phase current/voltage and machine phase currents I_A, I_V. (b) I_x, I_y, torque and DC bus voltage. (c) Subspace currents I_a, I_b, I_{01}, and I_{02}.

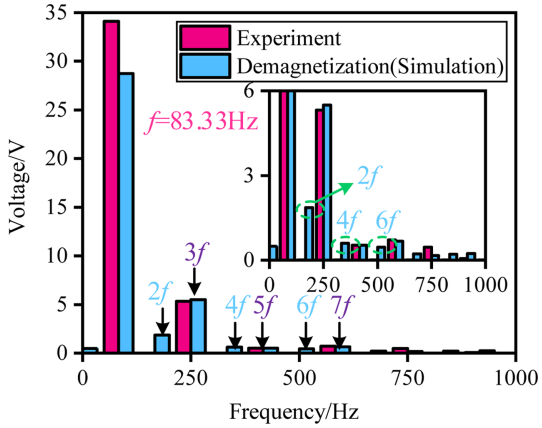

Fig. 14. (Color online) Simulation and experimental results of the input voltage's frequency spectrums under normal and demagnetized conditions.

operation (experimental results) are presented in Fig. 14. It is evident that the input voltage spectrum of the machine after demagnetization exhibits the 2nd and 4th harmonics while the magnitude of the fundamental harmonic is reduced. Conversely, during the experiment, even-order harmonics are not observed in the input voltage spectrum, indicating an absence of irreversible demagnetization in the machine. The experiment was conducted under ambient conditions at a temperature of 25°C, rendering it impracticable to verify the worst scenario. The analysis suggests that there is no immediate jeopardy of demagnetization as long as the operating temperature remains within safe thresholds.

The analysis presented thus far for the in-motion charging mode considers a steady-state operating point. However, in a real-world EV application, the propulsion system operates over a dynamic drive cycle, characterized by varying speed and torque demands. These variations have direct implications for the charging performance and electromagnetic stresses discussed. For instance, during high-torque acceleration phases, the propulsion currents increase, which would likely exacerbate the PM demagnetization risk when superimposed on the DC-biased field from the charging current. Conversely, during cruising or regenerative braking, the lower torque demand and different current phase angles might temporarily reduce the combined magnetic stress. Therefore, while the steady-state analysis at a representative operating point (1000 RPM, 12A) provides critical insights into the inherent risks, a comprehensive assessment of the MEI-EDROC's reliability would require future investigation under entire standard drive cycles to identify the most critical operating conditions.

6. Conclusion

In this paper, the electromagnetic performances of the MEI-EDROC are evaluated. And the system is verified on a 2kW prototype. Based on the above findings, several key engineering guidelines for the design of MEI-EDROC systems can be derived:

(1) To ensure mechanical safety during stationary charging (DC and single-phase modes), the rotor should be positioned at predetermined angles where the harmonic-induced torque is minimized.

(2) For in-motion charging, active control strategies to suppress the torque ripple introduced by the ZSC are necessary to ensure smooth operation and mechanical integrity.

(3) Thermal management is critical, especially for high-power charging modes like three-phase charging and in-motion charging. The operating temperature must be strictly controlled below the critical point (e.g., 130°C) to prevent irreversible demagnetization, potentially requiring derating strategies or enhanced cooling solutions.

(4) The significant PM eddy loss in three-phase charging mode highlights the importance of PM segmentation or the use of low-loss magnet materials in the machine design phase to maintain high system efficiency.

(5) The electromagnetic performance evaluation in this paper establishes a foundational understanding at key operating points. However, the interaction between dynamic propulsion demands dictated by EV drive cycles and the charging process, particularly in the in-motion charging mode, necessitates further research. Future work should involve testing or simulating the MEI-EDROC over standard drive cycles to quantify the cycle-average losses and to identify the transient operating points that pose the highest risk of demagnetization. This will lead to more robust and relevant design guidelines and online control strategies for thermal and demagnetization management.

References

[1] Y. Zhang, J. Fang, F. Gao, S. Gao, D. J. Rogers, and X. Zhu, IEEE Trans. Power Electron. **36**, 1717 (2021).
[2] D. B. Wickramasinghe Abeywardana, P. Acuna, B. Hredzak, R. P. Aguilera, and V. G. Agelidis, IEEE Trans. Power Electron. **33**, 3462 (2018).
[3] R. Hou and A. Emadi, IEEE Trans. Power Electron. **32**, 1860 (2017).
[4] J. Gao, W. Sun, D. Jiang, Y. Zhang, and R. Qu, IEEE Trans. Power Electron. **36**, 4752 (2021).
[5] S. Sharma, M. V. Aware, and A. Bhowate, IEEE Trans.

Transp. Electrification **6**, 83 (2020).
[6] M. Tong, M. Cheng, W. Hua, and S. Ding, IEEE Trans. Veh. Technol. **69**, 3793 (2020).
[7] S. Wang and P. W. Lehn, IEEE Trans. Transp. Electrification **8**, 82 (2022).
[8] H. J. Raherimihaja, Q. Zhang, T. Na, M. Shao, and J. Wang, IEEE Trans. Power Electron. **35**, 12122 (2020).
[9] I. Subotic, N. Bodo, E. Levi, B. Dumnic, D. Milicevic, and V. Katic, IET Electr. Power Appl. **10**, 217 (2016).
[10] A. Hemeida, M. Y. Metwly, A. S. Abdel-Khalik, and S. Ahmed, Energies **14**, 1848 (2021).
[11] Y. Xiao, C. Liu, and F. Yu, IEEE Trans. Power Electron. **35**, 2776 (2020).
[12] A. Habib, A. Shawier, M. S. Abdel-Majeed, A. S. Abdel-Khalik; M. S. Hamad, and R. A. Hamdy, IEEE Trans. Power Electron. **37**, 8345 (2022).
[13] Z. Ullah, M. Y. Metwly, A. Hemeida, A. S. Abdel-Khalik, J. He, and S. Ahmed, IEEE Trans. Transp. Electrification **10**, 3334 (2024).
[14] F. Yu, Q. Yin, Z. Zhu, and X. Cheng, IEEE Trans. Power Electron. **39**, 4050 (2024).
[15] C. Zhang, C. Gan, K. Ni, Z. Yu, Y. Chen, and H. Shi, IEEE Trans. Ind. Electron. **70**, 2351 (2023).
[16] M. Nakano, H. Kometani, and M. Kawamura, IEEE Trans. Ind. Appl. **42**, 429 (2006).
[17] H.-K. Kim and J. Hur, IEEE Trans. Ind. Appl. **53**, 982 (2017).
[18] W. Li, G. Feng, C. Lai, Z. Li, J. Tian, and N. C. Kar, IEEE Trans. Ind. Appl. **55**, 5204 (2019).
[19] E. L. BRANCATO, IEEE Trans. Elec. Insul. **EI-13**, 308 (1978).
[20] X. Ding, J. Liu, and C. Mi, in 2011 6th IEEE Conference on Industrial Electronics and Applications, Beijing, China: IEEE, 179 (2011).
[21] V. Ghorbanian, S. Hussain, S. Hamidizadeh, R. Chromik, and D. Lowther, IEEE Trans. Magn. **54**, 1 (2018).
[22] F. Yu, Z. Zhu, X. Liu, and Z. Zhang, IEEE Trans. Power Electron. **37**, 6544 (2022).